# We are IntechOpen, the world's leading publisher of Open Access books Built by scientists, for scientists

**4,800**
Open access books available

**122,000**
International authors and editors

**135M**
Downloads

Our authors are among the

**154**
Countries delivered to

**TOP 1%**
most cited scientists

**12.2%**
Contributors from top 500 universities


WEB OF SCIENCE™

Selection of our books indexed in the Book Citation Index in Web of Science™ Core Collection (BKCI)

## Interested in publishing with us?
## Contact book.department@intechopen.com

Numbers displayed above are based on latest data collected.
For more information visit www.intechopen.com

# 10

# Thermal Approaches to Interpret Laser Damage Experiments

S. Reyné[1], L. Lamaignère[2], J-Y. Natoli[3] and G. Duchateau[4]
[1,2]*Commissariat à l'Energie Atomique, Centre du Cesta*
*Avenue des Sablières, Le Barp*
[3]*Institut Fresnel, UMR-CNRS D.U. St Jérôme, Marseille*
[4]*Commissariat à l'Energie Atomique, Centre du Ripault, Monts*
*France*

## 1. Introduction

Laser-Induced Damage (LID) resistance of optical components is under considerations for Inertial Confinement Fusion-class facilities such as NIF (National Ignition Facility, in US) or LMJ (Laser MegaJoule, in France). These uncommon facilities require large components (typically $40 \times 40$ cm$^2$) with high optical quality to supply the energy necessary to ensure the fusion of a Deuterium-Tritium mixture encapsulated into a micro-balloon. At the end of the laser chain, the final optic assembly is in charge for the frequency conversion of the laser beam from the 1053 nm ($1\omega$) to 351 nm ($3\omega$) before its focusing on the target. In this assembly, frequency converters in $KH_2PO_4$ (or KDP) and DKDP (which is the deuterated analog), are illuminated either by one wavelength or several wavelengths in the frequency conversion regime. These converters have to resist to fluence levels high enough in order to avoid laser-induced damage. This is actually the topic of this study which interests in KDP crystals laser damage experiments specifically. Indeed, pinpoints can appear at the exit surface or most often in the bulk of the components. This is a real issue to be addressed in order to improve their resistance and ensure their nominal performances on a laser chain.

KDP crystals LID in the nanosecond regime, as localized, is now admitted to occur due to the existence of precursors defects (Demos et al., 2003; Feit & Rubenchik, 2004) present in the material initially or induced during the laser illumination. Because these precursors can not be identified by classical optical techniques, their size is supposed to be few nanometers. Despite the several attempts to identify their physical and chemical properties (Demos et al., 2003; Pommiès et al., 2006), their exact nature remains unknown or their role in the LID mechanisms is not clearly established yet. From the best of our knowledge, the main candidates to be proposed are linked to hydrogen bonds (Liu et al., 2003;?; Wang et al., 2005) which may induce point defects. Indeed, atomic scale defects such as interstitials or oxygen vacancies may be responsible for LID in KDP crystals. Also, point defects can migrate into structural defects (such as cracks, dislocations...) to create bigger defects (Duchateau, 2009). In the literature, many experimental and theoretical studies have been performed to explain the LID in KDP crystal (Demos et al., 2010; Duchateau, 2009; Duchateau & Dyan, 2007; Dyan et al., 2008; Feit & Rubenchik, 2004; Reyné et al., 2009; 2010). These studies highlight the

great improvements obtained in the KDP laser-induced damage field but also the difficulties to refine its understanding.

This chapter presents an overview of the LID in KDP when illuminated by a nanosecond laser beam. A review of the thermal approaches which have been developed over the last ten years is proposed. In Section 2, a description of two models including the heat transfer in defects of sub-micrometric size is carried out. We first propose a description of the DMT (Drude - Mie - Thermal) model (Dyan et al., 2008) which considers the incident laser energy absorption by a plasma ball (i.e. an absorbing zone), that may lead to a damage. Then, we describe a model coupling statistics and heat transfer (Duchateau, 2009; Duchateau & Dyan, 2007) which indicates that LID may be induced by the thermal cooperation of point defects. These two models are based on the resolution of the standard Fourier's equation where the features of the model under considerations are included. Also, the damage occurrence is determined according to a criterion defined by a critical temperature, which corresponds to the temperature reached by the defect to induce a damage site.

The previous models account for most of the classical results and trends on KDP LID published in the literature. In Section 3, some applications of these models are presented to interpret several sets of new experimental results. To interpret these new results, these thermal models have been adapted. First in the mono-wavelength case, it is shown that the DMT model accounts for the influence of the crystal orientation on the LID by considering defects with an ellipsoid geometry (Reyné et al., 2009). Then, when a KDP crystal is illuminated by two different wavelengths at the same time, it exists a coupling effect between the wavelength that induces a drastic drop in the laser damage resistance of the component. The model then addresses the resolution of the Fourier's equation by taking into account the presence of two wavelength at the same time (Reyné et al., 2010).

## 2. Review of thermal approaches to model LID

Section 2 presents different thermal approaches to explain the main results of laser-induced damage in KDP crystals. This section aims at giving a review of the last attempts to model laser-induced damage in KDP crystals (Duchateau & Dyan, 2007; Dyan et al., 2008). Modeling is mainly based on the resolution of the Fourier's equation on a precursor defect whose optical properties have to be characterized. Heat transfer in the KDP lattice may be considered either as the result of individual defects or as the cooperation of several point defects. These models can thus help to obtain more information on precursor defects and identify them.

### 2.1 DMT model

Since this study deals with conditions where the temperature evolution is strongly driven by thermal diffusion mechanisms, LID modeling attempts have to be based on the resolution of the Fourier equation. This has been first studied by Hopper and Uhlmann (Hopper & Uhlmann, 1970). Walker *et al.* improved the latter model by introducing an absorption efficiency that depends on the sphere radius (Walker et al., 1981). In this work, they considered only particular cases of the general Mie theory (Van de Hulst, 1981). Always on the basis of a heat transfer driven temperature evolution, Sparks and Duthler refined the characterization of the absorbing properties of the plasma through a Drude model but did not take into account the influence of the plasma ball radius (Sparks et al., 1981). In all these works, no importance has been given to the scaling law exponent $x$ linking the laser pulse density energy $F_c$ to the pulse duration $\tau$ as $F_c = \alpha\tau^x$ where $\alpha$ is a constant. Indeed, this temporal scaling law has motivated many research groups in order to obtain information on the mechanisms

responsible for laser-induced damage in dielectrics. Unlike the standard 0.5 value of $x$ that has been demonstrated in a lot of materials by both experimental (Stuart et al., 1996) and simple physical considerations (Bliss, 1971; Feit & Rubenchik, 2004; Wood, 2003), LID in KDP exhibits a lower value of $x$ that is close to 0.35 at $3\omega$ (Adams et al., 2005; Burnham et al., 2003). A first attempt has been made by Feit and co-workers to explain this deviation from 0.5 (Feit & Rubenchik, 2004; Trenholme et al., 2006). Hereafter, in the tradition of the state-of-the-art above-mentioned thermal modeling, an introduction to the general model is done. This model that takes into account all relevant physical mechanisms involved in LID in order to predict $x$ values that depart from the standard 0.5. Under a few assumptions, this is achieved by coupling a Drude model, the Mie theory and Thermal diffusion. The resulting model hereafter referred to as DMT is presented in Sec. 2.1.1. It allows to predict the values of $F_c$ and $x$ with respect to the optical constants of the plasma (see Sec. 2.1.3). The inverse problem (Gallais et al., 2004) is considered in order to determine the modeling physical parameters from experimental data. It permits to draw up conclusions about the electronic plasma density. Further, the evolution of the scaling law exponent is studied with respect to the laser pulse duration interval that is used to evaluate it.

#### 2.1.1 Thermal modeling and absorption efficiency

Since LID consists of a set of pinpoints distributed randomly within the bulk (Adams et al., 2005), the model considers the heating of a set of plasma balls whose radius varies from a few nanometers to hundreds of nanometers (Feit & Rubenchik, 2004). The main assumptions of the model are the following :

- continuity of the size distribution, i.e. it exists at least one sphere for each size,
- since it deals with a plasma, a high thermal conductivity of the absorbing sphere is assumed. It follows that the temperature is constant inside the plasma,
- the absorption efficiency is independent of time, i.e. it is assumed that the plasma reaches its stationary state in a time much shorter than the laser pulse duration,
- when the critical temperature $T_c$ is reached at the end of the pulse, an irreversible damage occurs,
- the physical parameters do not depend on the temperature.

The heating model for one sphere is based on the standard diffusion equation (Feit & Rubenchik, 2004; Hopper & Uhlmann, 1970) that can be written in spherical symmetry as :

$$\frac{1}{D}\frac{\partial T}{\partial t} = \frac{1}{r^2}\frac{\partial}{\partial r}(r^2\frac{\partial T}{\partial r}) \tag{1}$$

where $T$ is the temperature, $r$ is the radial coordinate and $D$ is the bulk thermal diffusivity defined as $D = \frac{\lambda_t}{\rho C}$ with $\lambda_t$, $\rho$, $C$ being the thermal conductivity, the density and the specific heat capacity of the KDP bulk respectively. Eq. (1) is solved under the following initial and boundary conditions :

i. at $t = 0$, $T = T_0 =$ constant $\forall\ r$, where $T_0$ is the initial ambient temperature set to 300 $K$,

ii. $T$ tends to $T_0$ when $r$ tends to infinity,

iii. the following enthalpy conservation at the interface between the bulk and the absorber is considered:

$$\frac{4\pi}{3}a^3\rho_p C_p\frac{\partial T}{\partial t}\Bigg]_{r=a} = I_0 Q_{abs}(m,y)\pi a^2 + 4\pi a^2\lambda_t\frac{\partial T}{\partial r}\Bigg]_{r=a} \tag{2}$$

where $a$, $\rho_p$ and $C_p$ are the radius, the density and the specific heat capacity of the absorber respectively. $Q_{abs}(m,y)$ is defined as the absorption efficiency that can be evaluated through the Mie theory (Van de Hulst, 1981). $m$ is the complex optical index of the absorber related to the one of the bulk and $y$ is the size parameter. Finally, $I_0$ is the laser intensity that is assumed to be constant with respect to time in order to correspond to an experimental top hat temporal profile.

Eq. (1) can be solved in the Laplace space (Carslaw & Jaeger, 1959) and the use of the initial and boundary conditions leads to the following solution for $r = a$ :

$$T(a,\tau) = T_0 + \frac{Q_{abs} I_0 \sqrt{4D\tau}}{4\lambda_t} \xi(U,A) \tag{3}$$

with

$$\xi(U,A) = \frac{UA}{1-X^2}\left(\phi(\frac{X}{A}) - X^2\phi(\frac{1}{XA})\right) \tag{4}$$

where $U = \sqrt{\frac{\kappa}{D}}$, $X = U + \sqrt{U^2-1}$ and $A = \frac{a}{\sqrt{4\kappa\tau}}$ are dimensionless. Note that $\xi(U,A)$ is a function that gives acoount for the material properties. The notation $\kappa = \frac{3\lambda_t}{4\rho_p C_p}$ is also introduced and has units of a thermal diffusivity, but mixes the properties of the bulk and the absorber. The function $\phi$ is defined as $\phi(z) = 1 - \exp(z^2)\ \mathrm{erfc}(z)$ where erfc is the complementary error function. Also, the fluence can be written as $F = I_0\tau$ which allows Eq. 3 to be re-formulated. The plot of $F$ as a function of $a$ exhibits a minimum (Hopper & Uhlmann, 1970) (see Fig. 1) and since the existence of at least one absorber of size $a$ is assumed, the critical fluence necessary to reach the critical temperature $T_c$ (set to 10000 $K$ in all the calculations (Carr et al., 2004)) can thus be written as :

$$F_c = \frac{2\lambda_t(T_c - T_0)}{Q_{abs}(a_c)\sqrt{D}} \frac{\sqrt{\tau}}{\xi(U,A_c)} \tag{5}$$

where $a_c$ is the radius that corresponds to the minimum fluence to reach $T_c$.
Moreover, for the case where $Q_{abs}$ does not depend on $a$, one can show from Eq. (5) and Fig. 1 that the critical fluence reaches a minimum for the critical radius $a_c$ :

$$a_c(\tau) = 2\sqrt{\kappa\tau}\, B(U) \tag{6}$$

where $B$ is a function of $U$. It can be shown that $B(\infty) = 1$ and $B(0) \simeq 0.89$. Elsewhere, the function $B(U)$ has to be evaluated numerically. If $Q_{abs}$ does not depends on $a$, then $x = 1/2$. It is worth noting that the value of $x$ can be refound from considerations about the enthalpy conservation at the interface.

The second step consists in showing by simple considerations how the introduction of the Mie theory permits to deviate from the standard $x = 1/2$ value. From that theory, $Q_{abs}$ depends on the sphere radius. More precisely, one can reasonably write $Q_{abs} \propto a_c^{\delta}$ where $\delta \in [-1;1]$. $\delta = -1$ corresponds to the case $a_c > \lambda$ and large values of the imaginary part $k$ of the optical index (typically a few unities as for metals) whereas $\delta = 1$ corresponds to the Rayleigh regime ($a_c \ll \lambda$). As above mentioned, $a_c$ is a function of the pulse duration that can be written as $a_c \propto \tau^{\gamma}$ where $\gamma$ is close to $1/2$. It follows that $F_c \propto \tau^{1/2-\delta\gamma}$ with $-1/2 \leq \delta\gamma \leq 1/2$ and therefore $x$ lies in the range $[0;1]$.

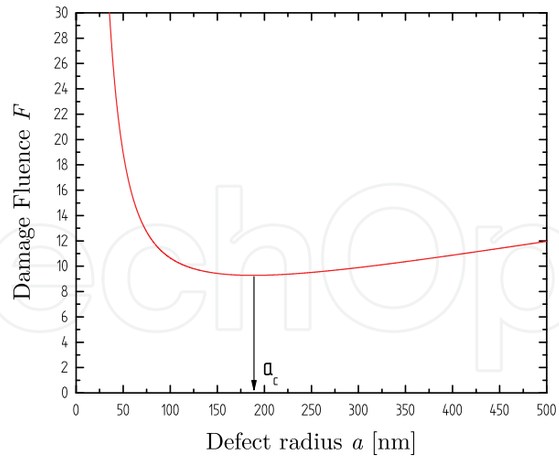


Fig. 1. Evolution of the damage fluence $F_c$ as a function of the defect size $a$. A minimum is obtained for $a = a_c$ which is associated to the critical fluence $F_c$.

#### 2.1.2 Determination of the plasma optical indices within the Drude model framework

Since the laser absorption is due to a plasma state, for which free electrons oscillate in the laser electric field and undergo collisions with ions, the optical indices of the plasma can be derived from the standard Drude model with damping (see for example Hummel (2001)). In that framework, the response of the electron gas to the external laser electric field is given by the following complex dielectric function :

$$\varepsilon = 1 - \frac{\omega_p^2}{\omega(\omega - i/\tau_{coll})} = \varepsilon_1 - i\varepsilon_2 \tag{7}$$

In this expression, $\omega_p$ is the electron plasma frequency given by $\omega_p = (n_e e^2/\varepsilon_0 m_*)^{1/2}$ where $n_e$ is the free electrons density and $m_*$ is the effective mass of the electron. $\tau_{coll}$ stands for the collisional time, i.e. the time elapsed between two collisions with ions. The dielectric function is linked to the complex optical index $m = n - ik$ by the relation $m^2 = \varepsilon$. It follows that $\varepsilon_1 = n^2 - k^2$ and $\varepsilon_2 = 2nk$. In the case where $m$ and hence $\varepsilon$ are known, the characteristic parameters of the plasma $n_e$ and $\tau_{coll}$ can be determined by inversing Eq. (7). The laser-induced electron density cannot exceed a critical value $n_c$ above which the plasma becomes opaque. This critical density is determined setting $\omega_p$ to $\omega$, which leads to $n_c = m_* \epsilon_0 \omega^2 / e^2$. In the next section, we will see that it is of interest to know the values of the optical index satisfying the physical requirement $n_e \leq n_c$ (or equivalently $\omega_p \leq \omega$) appearing in laser-induced experiments. By setting $n_e$ to $n_c$, the couples $(\varepsilon_1, \varepsilon_2)$ have to satisfy $(\varepsilon_1 - 1/2)^2 + \varepsilon_2^2 = (1/2)^2$ that is nothing but the equation of a circle centered at $(1/2, 0)$ and of radius $1/2$. Each point inside the circle satisfies the required condition $n_e \leq n_c$.

#### 2.1.3 Results

A description of the procedure that is used to compute all physical parameters of interest for the present paper is done first. For given pulse duration and $(n, k)$ values, the plot of the fluence required to reach the critical temperature $T_c$ as a function of the absorber radius – the plot that exhibits a minimum $a_c$ (Feit & Rubenchik, 2004) – allows to determine the critical

fluence $F_c$, i.e. the fluence for which the first damage appears. It is also possible to associate the critical Mie absorption efficiency $Q_{abs}(a_c)$ evaluated for $a = a_c$. In order to determine the scaling law exponent $x$ corresponding to a couple $(n,k)$, one only has to apply the last procedure for different pulse durations. It is then assumed that one can write $F_c = A\tau^x$ and the values of the parameters $A$ and $x$ are determined with a fitting procedure based on a Levenberg-Marquardt algorithm (*Numerical Recipies*, n.d.).
Now, within this modeling framework, the optical constants of the plasma can be determined by using experimental data that provide $F_c$ and $x$. To do so, by applying the above-described procedure, the theoretical evolution of $F_c$ and $x$ have been evaluated as a function of $(n,k)$ on Figs. 2 (a) and 2 (b) respectively. Fig. 2 (a) has been obtained with $\tau = 3\ ns$ whereas, for Fig. 2 (b), $\tau$ varies in the interval $[1.\ ns\ ; 10.\ ns]$ which is used experimentally (Burnham et al., 2003). The particular behavior of $F_c$ can be explained in a simple way. From Eq. (5), $F_c$ is proportional to $1/Q_{abs}$, $Q_{abs}$ being itself proportional to $\varepsilon_2 = 2nk$ since it deals with conditions close to the Rayleigh regime (Van de Hulst, 1981) ($a_c \simeq 100\ nm$ and thus $a/\lambda < 1$) and $\varepsilon_2 \ll 1$. Iso-fluence curves as shown on Fig. 2 (a) correspond to $F_c = \text{const}$, that is to say $1/Q_{abs} = \text{const}$ and subsequently $k \propto 1/n$. This hyperbolic behavior is all the more pronounced that $\tau$ is short. As regards the scaling law exponent, the main feature appearing on Fig. 2 (b) is that $x$ depends essentially on $k$, this trend becoming more pronounced as $k$ goes up. Indeed, for large enough values of $k$ whatever the value of $n$, the shape of $Q_{abs}$ with respect to $a$ remains almost the same that imposes the value of $x$. Now, the optical constants can be determined from experimental data $F_c = 10 \pm 1\ J/cm^2$ (Carr et al., 2004) and $x = 0.35 \pm 0.05$ (Burnham et al., 2003). The theoretical index range providing these two values is obtained by performing a superposition of Figs. 2 (a) and 2 (b) as shown on Fig. 2 (c). In addition, the intersection region is restricted by the above-mentioned condition $\omega_p \leq \omega$. Since the uncertainty on $F_c$ is relatively small, the shape of the intersection region is elongated. The extremal points in the $(n,k)$ plane are roughly $(0.16, 0.16)$ ($n_e = n_c$ and $\tau_{coll} = 3.50$ fs) and $(0.40, 0.06)$ ($n_e = 0.84 n_c$ and $\tau_{coll} = 3.27$ fs). The optical index satisfying $F_c = 10\ J.cm^{-2}$ and $x = 0.35$ is $(0.22, 0.12)$ ($n_e = 0.97 n_c$ and $\tau_{coll} = 3.40$ fs). Also, we find values of $n_e$ and $\tau_{coll}$ that are close to the plasma critical density and the standard femtosecond range respectively. It is worth noting that the associated Mie absorption efficiency with the latter optical indices is $Q_{abs}(a_c) = 6.5\ \%$ where $a_c \simeq 100\ nm$. In order to compare to experiments where the ionized region size is estimated to $30\ \mu m$ (Carr et al., 2004) in conditions where the fluence is twice the critical fluence (for such a high energy, the plasma spreads over the whole focal laser spot), we have evaluated $Q_{abs}$ with the above found index and $a = 30\ \mu m$. In that case, $Q_{abs} \simeq 10\ \%$ which is close to the 12 % experimental value (Carr et al., 2004). It is noteworthy that $Q_{abs}$ saturates with respect to $a$ for such values of the optical index and absorber size.

### 2.2 Coupling statistics and heat tranfer

In order to characterize experimentally the resistance of KDP crystals to optical damaging, a standard measurement consists in plotting the bulk damage probability as a function of the laser fluence $F$ (Adams et al., 2005) that gives rise to the so-called S-curves. In order to explain this behavior, thermal models based on an inclusion heating have been proposed (Dyan et al., 2008; Feit & Rubenchik, 2004; Hopper & Uhlmann, 1970). In these approaches, statistics (Poisson law) and inclusion size distributions are assumed. On the other hand, pure statistical approaches mainly devoted to the onset determination and that do not take into account thermal processes have been considered (Gallais et al., 2002; Natoli et al., 2002; O'Connell, 1992; Picard et al., 1977; Porteus & Seitel, 1984). On the basis of the above-

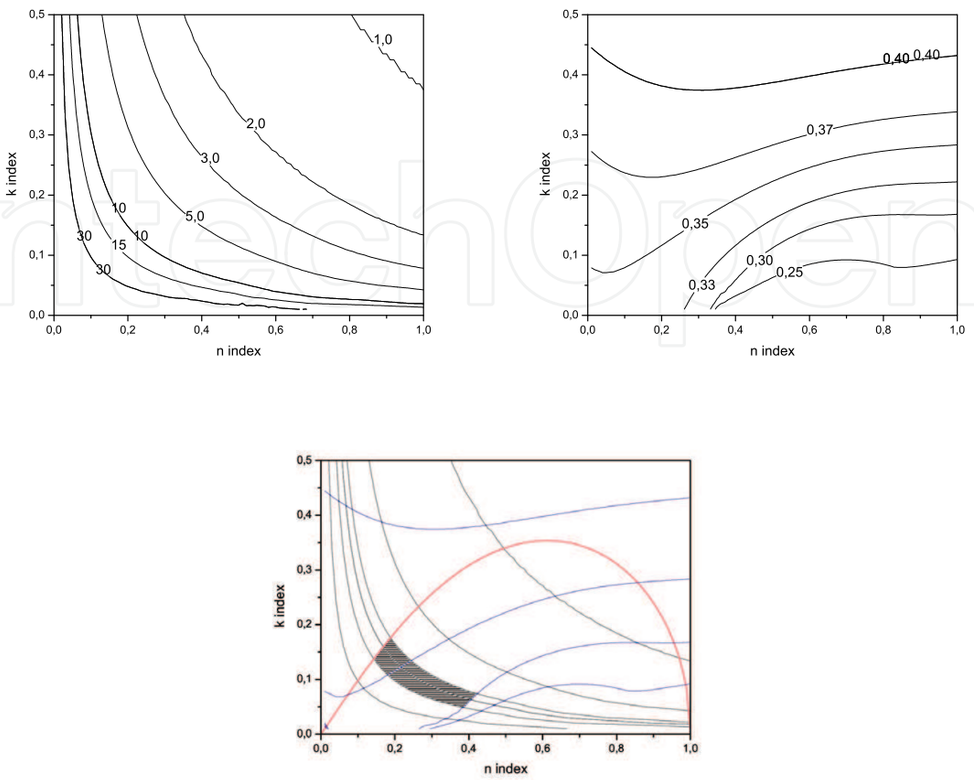


Fig. 2. (top left) Critical fluence $F_c$ in $J.cm^{-2}$ as a function of $n$ and $k$ for $\tau = 3\ ns$. (top right) Scaling law exponent $x$ as a function of $n$ and $k$ for $\tau \in [1.\ ns;\ 10.\ ns]$. (bottom) Intersection of (a) and (b), the highlighted area delimits the region satisfying experimental data.

mentioned assumption of defects aggregation, this section proposes a model where Absorbing Defects of Nanometric Size, hereafter referred to as ADNS, are distributed randomly and may cooperate to the temperature rise $\Delta T$ through heat transfer within a given micrometric region of the bulk that corresponds to an heterogeneity. Since this approach combines statistics and heat transfer, it allows to provide the cluster size distribution, damage probability as a function of fluence, and scaling laws without any supplementary hypothesis. The present section aims at introducing the general principle of this model and giving first main results that are compared with experimental facts. A particular attention has been payed to scaling laws since they are very instructive in terms of physical mechanisms. More precisely, a deviation from the standard $\tau^{1/2}$ law has recently been observed within KDP crystals (Adams et al., 2005) and this model (as the DMT one previously presented) also proposes a plausible explanation of this fact based on thermal cooperation effects and statistics. Despite the 2D and 3D representation was tackled (Duchateau, 2009; Duchateau & Dyan, 2007), this section focuses on a one dimensional modeling that gives a good insight about physics and seems to provide a nice counterpart to experimental tendencies.

This section is organized as follows: Sec. 2.2.1 deals with the model coupling statistics and heat transfer. In a first part, the principle of the approach is exposed. Secondly, numerical

predictions of the model are provided in terms of damage probability S-curves and temporal scaling laws. Results are discussed and compared with experimental facts in Sec. 2.2.2.

#### 2.2.1 Random distribution of absorbing defects

This model considers a set of ADNS that are distributed on a spatial domain. When a crystal cell contains a defect, it is called an alterate cell which may absorb laser energy much more efficiently than a pure cell crystal. Therefore, from heat transfer point of view, the alterate cell may be seen as a very tiny source inducing temperature rising. This source of size $a$ is assumed to be close to the characteristic crystal cell dimension, i.e. one nanometer. Within a 1D framework, the domain of size $Na$, that is assumed to correspond to an heterogeneity, then is composed of two kinds of cells. The temperature evolution is governed by the Fourier's equation:

$$\frac{\partial T}{\partial t} = D\frac{\partial^2 T}{\partial x^2} + \frac{A}{\rho C}\sum_{i=1}^{n_{ADNS}} \Pi(x - x_i) \tag{8}$$

where $x_i \in [0, Na]$ stands for the position of ADNS or alterate cells whose number is $n_{ADNS}$ and $A$ is the absorbed power per unit of volume. Material physical parameters such as thermal diffusivity $D$ and conductivity $\lambda$, density $\rho$ or specific heat capacity $C$, linked by the relation $D = \lambda/\rho C$, are assumed to remain constant in the course of interaction. The function $\Pi$ is defined as follows:

$$\begin{cases} \Pi(x) = 1 \text{ if } x \in [x - a/2; x + a/2] \\ \Pi(x) = 0 \text{ elsewhere} \end{cases} \tag{9}$$

The way to distribute defects is addressed in the next paragraph. A general solution of (8) is given by (Carslaw & Jaeger, 1959):

$$T(x,t) = T_0 + \sum_{i=1}^{n_{ADNS}} \Delta T^{(i)}(x,t) \tag{10}$$

where $T_0 = 300K$ is the initial temperature of the crystal and where the temperature rise $\Delta T^{(i)}(x,t)$ induced by one ADNS is solution of the following equation:

$$\frac{\partial \Delta T^{(i)}}{\partial t} = D\frac{\partial^2 \Delta T^{(i)}}{\partial x^2} + \frac{A}{\rho C}\Pi(x - x_i) \tag{11}$$

Now, since conditions are $a \ll \sqrt{Dt}$ (for $D_{KDP} = 6.5 \times 10^{-7} m^2.s^{-1}$ and $\tau = 1ns$, it leads to $\sqrt{Dt} \simeq 25nm$), in order to deal with simple formula allowing fast numerical calculations, the function $\Pi(x)$ is replaced by the Dirac delta function $\delta(x)$, i.e.it is imposed that the energy absorbed by a finite-size defect is in fact absorbed by a point source. The ADNS then may be seen as a heating point source. Within this framework, a good approximated solution of Eq. (11) is given by:

$$\theta_{1D}(x,t) = \frac{Aa}{2\lambda}\left\{2\left(\frac{Dt}{\pi}\right)^{1/2}\exp\left(-\frac{x^2}{4Dt}\right) - x\,\mathrm{erfc}\left(\frac{x}{2\sqrt{Dt}}\right)\right\} \tag{12}$$

The reliability of this approximation has been checked by performing a full numerical resolution of Eq. (8) based on a finite differences scheme. In order to illustrate the main principle of the model, Fig. 3 plots the evolution of the temperature (10) as a function of the 1D spatial coordinate in a case for which $n_{ADNS} = 15$, $A/\rho C = 10^{13} K.s^{-1}$ and $\tau = 1\ ns$. This

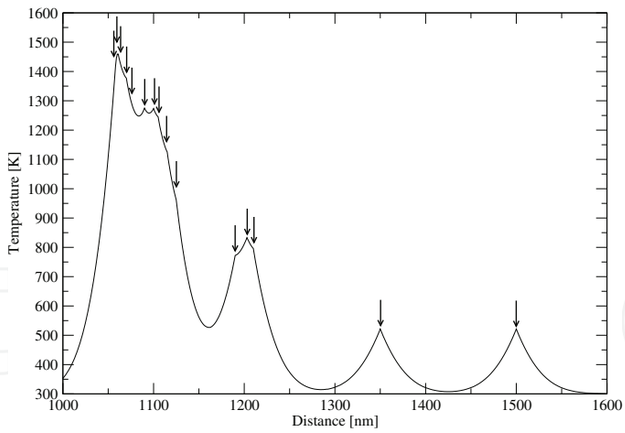


Fig. 3. Spatial temperature evolution resulting from a particular random throwing. 15 ADNS are present, $A/\rho C = 10^{13} K.s^{-1}$ and $\tau = 1\ ns$ are used. The temperature rise is enhanced when several ADNS aggregate. Defects positions are shown by vertical arrows.

graph shows a characteristic spatial behavior where it clearly appears that cooperative effect leads to a locally higher temperature.

From these calculations, it is then possible to construct a damage probability law. For a given fluence $F$, a number $n_{draw}$ of ADNS distribution are generated, and it is checked whether or not each ADNS distribution induces a temperature higher than the critical temperature $T_c$. Let $n_{dam}$ be the number of ADNS configurations leading to $T \geq T_c$. Then, the damage probability is simply given by $P(F) = n_{dam}(F)/n_{draw}$. In order to plot the damage probability as a function of fluence, the source term of Eq. (11) has to be evaluated. Since the defect nature is unknown, the absorbed power per unit of volume $A$ cannot be evaluated theoretically thus leading to an empirical evaluation from experimental data. From dimensional analysis, it can be written that $A = \xi F/l\tau$ where $\xi$ and $l$ may be identified to a dimensionless absorption efficiency and an effective cluster size respectively. In conditions where thermal diffusion is not taken into account, the temperature rise induced by the laser pulse reads $\Delta T = \Delta\rho_E/\rho C$ where $\Delta\rho_E = \xi F/l$ and $C = 0.023 \times 900 \simeq 2\ J.K^{-1}.cm^{-3}$ are the absorbed energy per unit of volume and the heat capacity per unit volume of KDP respectively. From black body measurements (Carr et al., 2004), it turns out that the temperature rise associated with damage induced by a $3ns$ laser pulse with $F \simeq 10 J.cm^{-2}$ is roughly $10000K$. That allows to estimate the unknown ratio $\xi/l$ to about $2 \times 10^3 cm^{-1}$. In fact, thermal diffusion processes take place, and $\xi/l$ must be higher. Therefore, we choose $\xi/l = 10^4 cm^{-1}$ and we will check in Sec. 2.2.2 that it is consistent with experimental data. Since we are working within the Rayleigh regime for which $\xi \propto l$ (defects clusters are assumed to be well smaller than $\lambda = 351nm$), it is assumed that $\xi/l$ to remain almost unchanged when $l$ varies. Also, the use of $A = 10^4 \times F/\tau$ as the source term empirical expression of Eq. (11) in numerical calculations is done.

In following calculations, critical temperature is fixed to $T_c = 5000\ K$ (Carr et al., 2004). The Laser-Induced Damage Threshold (LIDT) is then defined as the value of the fluence $F_c$ such that the damage probability equals 10%. As usually in Physics, this choice indicates actually the departure from perturbative conditions. It is worth noting that taking 5% or 20% will not affect the main conclusions of this model.

### 2.2.2 Results

Let us begin with the 1D case. The damage probability as a function of the laser fluence is shown on Fig. 4 for $\tau = 250ps$, $1ns$, $4ns$ and $16ns$. In all cases, we choose $n_{ADNS} = 100$, $N = 10000$ and statistics is supported by 200 drawings. The general shape of curves exhibits a standard behavior for which damage probabilities increase monotonically with the fluence. Further, calculations for $\tau = 3$ $ns$ show that the LIDT is close to 9 $J.cm^{-2}$ that is in a good agreement with Carr *et al.*'s experiment (Carr et al., 2004). Also, *a posteriori*, this result confirms the reliability of the evaluation of the coefficient $\xi/l$ that has been set to $10^4 cm^{-1}$. For a given pulse duration, probability becomes non-zero when, within at least one drawing, a group of ADNS is sufficiently aggregated to form a cluster whose size and density are enough to reach locally the critical temperature.

When the fluence goes up, the critical temperature may be reached by smaller or less dense cluster. Since they are in a larger number, the probability increases itself. A probability close to one corresponds to the lowest cooperative effect, i.e. involving the smallest number of ADNS around the place where $T \geq T_c$. This number is determined counting ADNS that contribute significantly to the place $x_c$ where $T \geq T_c$. To do so, the counting is made in the range $[x_c - 4\sqrt{D\tau}, x_c + 4\sqrt{D\tau}]$. It appears that, for a given pulse duration, the larger the fluence, the lesser the number of ADNS involved in the damage.

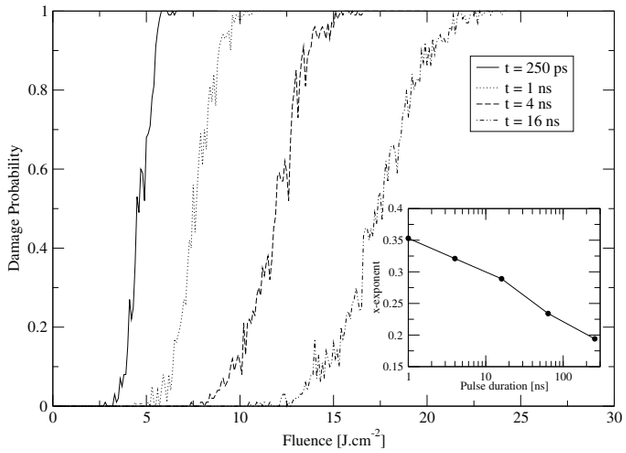


Fig. 4. Evolution of the damage probability as a function of fluence within the 1D model. Four pulse durations are considered : $\tau = 250ps, 1ns, 4ns$ and $16ns$. Parameters are $n_{ADNS} = 100$ and $N = 10000$. 200 drawings have been performed for each fluence. Sub-figure displays the scaling law exponent as a function of the pulse duration (see text).

Now, les us focus on the influence of the pulse duration on the damage probability curves and, more precisely, the scaling law linking the fluence to the pulse duration. Fig. 4 shows clearly that the LIDT is shifted towards higher fluence when $\tau$ increases. Actually, for long pulse, the thermal diffusion process is more efficient and more energy is needed to reach the critical temperature for a given ADNS configuration. For instance, the temperature rises as $\sqrt{\tau}$ (Carslaw & Jaeger, 1959) thus implying the scaling law $F_{c1}/F_{c2} = \sqrt{\tau_1/\tau_2}$. In order to establish the scaling law in our model, it is assumed that $F_{c1}/F_{c2} = (\tau_1/\tau_2)^x$ may be written. The exponent $x$ is determined from the knowledge of $F_{c1}$, $F_{c2}$, $\tau_1$ and $\tau_2$. In fact, $\tau_2 = 4\tau_1$ is stated and the $x$ exponent is evaluated as a function of $\tau_2$ ranging from 1 $ns$ to 16 $ns$. The values of $F_c$ and $x$ are displayed for the above-mentioned values of $\tau$ in Table 1. Note that more drawings than in Fig. 4 have been performed in order to determine $F_c$ with a correct

numerical precision. It appears that $x$ differs from the expected $1/2$ value and takes values

| | $F_c$ $[J.cm^{-2}]$ | $x$ |
|---|---|---|
| $\tau = 250ps$ | 3.85 | |
| $\tau = 1ns$ | 6.28 | 0.353 |
| $\tau = 4ns$ | 9.80 | 0.321 |
| $\tau = 16ns$ | 14.60 | 0.288 |

Table 1. Critical fluence and x-exponent as a function of the pulse duration

that depends on the pulse duration. For the sake of completeness, the values of $x$ for a large range of pulses ratios is plotted on sub-figure of Fig. 4. The evolution of $x$ can be fitted by the empirical following expression:

$$x = -\alpha \ln \tau + \beta \tag{13}$$

with $\alpha = 2.92 \times 10^{-2}$ and $\beta = 0.3592$. The fit error is close to 2% and may be due to statistical uncertainties. We have checked that a different ratio $\tau_2/\tau_1$ leads to the same general expression of $x$ but where the coefficients $\alpha$ and $\beta$ differ slightly. For a given ADNS spatial configuration, this behavior of $x$ can be understood by the following consideration: for a single ADNS, since $\Delta T \propto \tau^{1/2}$, the according scaling law reads $F_c \propto \tau^{1/2}$. For a given pulse duration, since several ADNS are involved, whose effective cluster size is non negligible in comparison with the diffusion length, the temperature goes up faster than $\tau^{1/2}$ and the scaling law exponent is accordingly lower than $1/2$. Now, when $\tau$ increases, since the contribution length is proportional to $\sqrt{D\tau}$, more and more defects take part in the temperature rise. It is like if the laser pulses *sees* different target sizes with respect to its duration. It then turns out that less energy is needed than in a situation where all target components always contribute for any interaction time. Consequently, the scaling law deviates from the standard $x = 1/2$ value as the pulse duration goes up.

## 3. Evolutions of the thermal models and interpretation of the experiments

Sec. 2 has presented different thermal approaches capable to explain the most of usual results of laser-induced damage in KDP crystals in the nanosecond range. Despite some approximations, these models allow a good interpretation of the complex scenario of KDP laser damage but do not include any polarization influence nor the presence of two laser pulses with different wavelengths. In this section, the latter influences are thus addressed. First, we focus on the effect of polarization on the laser damage resistance of KDP. Then we will highlight the effect of multiple wavelength interacting with the crystal simultaneously and the consequences on its resistance.

### 3.1 The effect of laser polarization on KDP crystal resistance: influence of the precursor defects geometry

#### 3.1.1 Experimental results at $1\omega$: laser damage density versus fluence and $\Omega$

*Test protocol*

Generally, laser damage tests yield to the Standard (*ISO Standard No 11254-1:2000; ISO Standard No 11254-2:2001*, 2001). The so-called 1-on-1 procedure has been used here to test the KDP crystal. Specific data treatments described in (Lamaignère et al., 2009) allow to extract the bulk damage densities as a function of fluence. This part interests more particularly in the effect of the polarization on KDP crystals resistance. Then the $\Omega$ notation is introduced

as the angle between the polarization of the incident laser beam and the propagation axis. In substance, $\Omega = 0°$ corresponds to the case where the laser polarization $\vec{E}$ is collinear to the ordinary axis of the crystal. When $\Omega = +90°$, $\vec{E}$ is collinear to the extraordinary axis of the crystal.

*Evolution of the laser damage density versus fluence*

Fig. 5 presents the evolution of the laser damage density as a function of $1\omega$ fluence. Tests have been performed for two orthogonal positions of the crystal, i.e. (a) the laser polarization along the ordinary axis (blue triangles), (b) the laser polarization along the extraordinary axis (red squares).

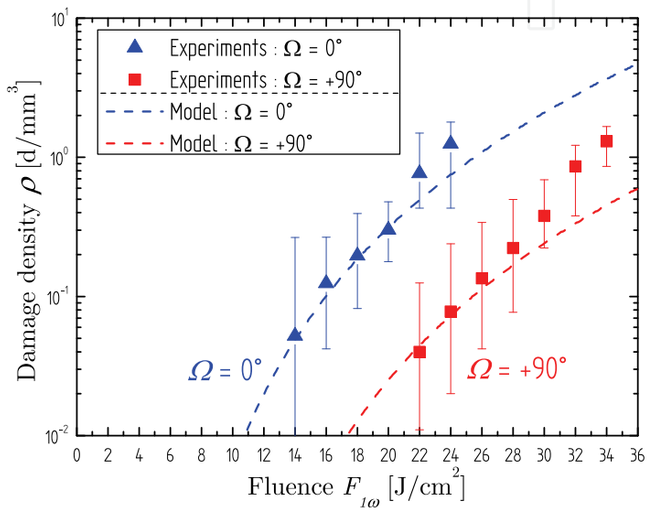


Fig. 5. Evolution of the laser damage density as a function of the $1\omega$ fluence. Blue triangles correspond experimental results for the ordinary position ($\Omega = 0°$) and red squares to extraordinary position ($\Omega = 90°$). Modeling results are represented in dash lines, respectively for each test positions. Modeling results are discussed in Sec. 3.1.3. Damage densities evolve as a power law of the fluence.

According to Fig. 5, results clearly appear different between the two positions as we can estimate a shift of about 10 J/cm$^2$. This implies a factor 1.4 - 1.5 on the fluence at constant damage density.

*Laser damage density versus $\Omega$ at $1\omega$*

Studying the laser damage density as a function of the rotation angle $\Omega$ has been carried out to investigate a potential effect due to fluence. It is worth noting that rotating the crystal is equivalent to turning the beam polarization. This test has been performed for two different fluences $F_{1\omega}$ (i.e. at 19 J/cm$^2$ and 24.5 J/cm$^2$). Note that the choice of these $F_{1\omega}$ test fluences allows scanning damage probabilities in the whole range [0 ; 1]. Fig. 6 illustrates the damage density as a function of $\Omega$. Red squares and blue triangles respectively correspond to tests carried out at $F_{1\omega} = 24.5$ J/cm$^2$ and at $F_{1\omega} = 19$ J/cm$^2$.

Fig. 6 highlights the influence of crystal orientation on LID. To address this point, one may interest in the variations of the damage density as a function of $\Omega$. In the range [0°, 90°], apart from the points referenced by the black arrows (see explanations after), it can be observed

that the laser damage density globally decreases in the range [0°, 90°]. If considering now the black arrows, these points correspond to local generation of SHG. It has been noticed that for these particular points (i.e. $\Omega = 40°$and $\Omega = 60°$) the laser damage density is punctually altered as an indication that SHG tends to cooperate to damage initiation.

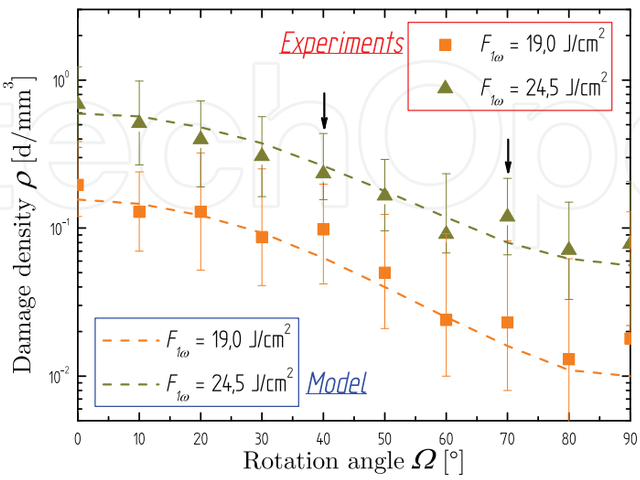


Fig. 6. Evolution of laser damage density as a function of Ω, for two different $1\omega$ fluences. Green triangles and orange squares respectively correspond to $F_{1\omega}$ = 19 J/cm$^2$ and $F_{1\omega}$ = 24.5 J/cm$^2$. Modeling results are represented in dash lines, respectively for each fluence. Modeling results are discussed in Sec. 3.1.3.

Many assumptions may be done to explain these observations. Crystal inhomogeneity, tests repeatability, self-focusing, walk-off and SHG (Demos et al., 2003; Lamaignère et al., 2009; Zaitseva et al., 1999;?) were suspected to be possible causes for these results due to their orientation dependence they may induce. But it has been ensured that these mechanisms were not the main contributors (even existing, participating or not) to explain the influence of polarization on KDP laser damage resistance. This assessment has to be nuanced in the case of SHG. These conclusions are also in agreement with literature relative to (non)-linear effects in crystals, qualitatively considering the same range of operating conditions (ns pulses, beams of few hundreds of microns in size, intensity level below a hundred GW/cm$^2$, etc).
To conclude on the experimental part, it is thus necessary to find another explanation (than SHG). This is addressed in the next section which introduces defects geometry dependence and proposes a modeling of the damage density versus fluence and Ω.

### 3.1.2 Modeling: coupling DMT and DDscat models

*DMT model*

The DMT code presented in Sec. 2.1 is capable to extract damage probabilities or damage densities as a function of fluence, i.e. directly comparable to most of experimental results. To do so, DMT model considers a distribution of independent defects whose size is supposed to be few tens of nanometers that may initiate laser damage. Considering that any defect leads to a damage site, damage density is obtained from Eq. (14):

$$\rho(F) = \int_{a\_(F)}^{a_+(F)} D_{def}(a).da \tag{14}$$

Where $[a_-(F), a_+(F)]$ is the range of defects size activated at a given damage fluence level, $D_{def}(a)$ is the density size distribution of absorbers assumed to be (as expressed in (Feit & Rubenchik, 2004)):

$$D_{def}(a) = \frac{C_{def}}{a^{p+1}} \tag{15}$$

Where $C_{def}$ and $p$ are adjusting parameters. This distribution is consistent with the fact that the more numerous the precursors (even small and thus less absorbing), the higher the damage density. In Sec. 2.1.1, Eq. (5) has defined the critical fluence $F_c$ necessary to reach the critical temperature $T_c$ for which a first damage site occurs, which can be written again as (Dyan et al., 2008):

$$F_c \propto \gamma \frac{T_c - T_0}{Q_{abs}(a_c)} \tau^x \tag{16}$$

Where $\gamma$ is a factor dependent of material properties, $T_0$ is the room temperature, $\tau$ is the pulse duration and $Q_{abs}$ is the absorption efficiency. What is interesting in Eq. (16) is the dependence in $Q_{abs}$. Eq. (16) shows that to deviate $F_c$ from a factor $\sim$1.5 (this value is observed on Fig. 5 between the two positions of the crystal), it is necessary to modify $Q_{abs}$ by the same factor. It follows that an orientation dependence can be introduced through $Q_{abs}$. It is then supposed that the geometry of the precursor defect can explain the previous experimental results.

*Geometries of defects*

As regards KDP crystals, lattice parameters $a$, $b$ and $c$ are such as $a = b \neq c$ conditions. The defects are assumed to keep the symmetry of the crystal so that the defects are isotropic in the $(ab)$ plane due to the multi-layered structure of KDP crystal. The principal axes of the defects match with the crystallographic axes. Assuming this, it is possible to encounter two geometries (either $b/c < 1$ or $b/c > 1$ ), the prolate (elongated) spheroid and the oblate (flattened) spheroid, represented on Fig. 7.

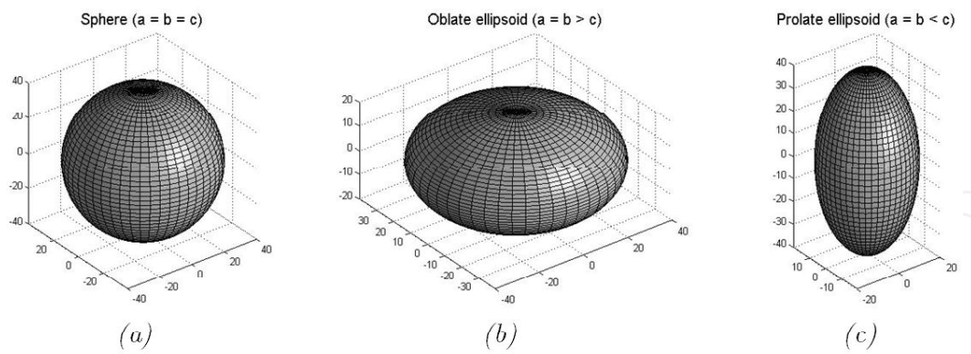


Fig. 7. Geometries proposed for modeling: (a) a sphere, which is the standard geometry used, (b) the oblate ellipsoid (flattened shape) and (c) the prolate ellipsoid (elongated shape). The value of the aspect ratio (between major and minor axis) is set to 2.

*DDScat model*

Defining an anisotropic geometry instead of a sphere implies to reconsider the set of equations (i.e. Fourier's and Maxwell's equations) to be solved. Concerning Fourier's equation, to our knowledge, it does not exist a simple analytic solution. So temperature determination remains solved for a sphere. This approximation remains valid as long as the aspect ratio does

not deviate too far from unity. This approximation will be checked in the next paragraph. As regards the Maxwell's equation, it does not exist an analytic solution in the general case. It is then solved numerically by using the discrete dipole approximation. We addressed this issue by the mean of DDScat 7.0 code developed by Draine and co-workers (Draine & Flatau, 1994; 2008; n.d.). This code enables the calculations of electromagnetic scattering and absorption from targets with various geometries. Practically, orientation, indexes from the dielectric constant and shape aspect of the ellipsoid have to be determined. One would note that SHG is not taken into account in this model since it has been shown experimentally in Sec. 3.1.1 that SHG does not contribute to LID regarding the influence of orientation.

*Parameters of the models*

The main parameters for running the DMT code are set as follow. Parameters can be divided into two categories: those that are fixed to describe the geometry of the defects (e.g. the aspect ratio) and those we adapt to fit to the experimental damage density curve for $\Omega = 0°$($T_c, n_1, n_2, C_{def}$ and $p$). The value of each parameter is reported in Table 2 and their choice is explained below. We assume a critical damage density level at $10^{-2}$ d/mm$^3$ (it is consistent with experimental results in Fig. 5 that it would be possible to reach with a larger test area). This criterion corresponds to a critical fluence $F_c$ = 11 J/cm$^2$ and a critical temperature $T_c$ = 6,000 K. This latter value agrees qualitatively with experimental results obtained by Carr *et al.* (Carr et al., 2004), other value (e.g. around 10,000 K) would not have significantly modified the results. Complex indices have been fixed to $n_1 = 0.30$ and $n_2 = 0.11$. $C_{def}$ and $p$ necessary to define the defects size distribution are chosen to ensure that damage density must fit with experimentally observed probabilities (i.e. $P = 0.05$ to $P = 1$).

| Critical damage density | $T_c$ | $n_1$ | $n_2$ | $C_{def}$ | $p$ | Aspect ratio | Rotation angle $\Omega$ |
|---|---|---|---|---|---|---|---|
| $10^{-2}$ d/mm$^3$ | 6,000 K | 0.30 | 0.11 | 5.5 $10^{-47}$ | 7.5 | 2 | 0 to 90° |

Table 2. Definition of the set of parameters for the DMT code at 1064 nm.

It is worth noting that these parameters have been fixed for $F_{1\omega}$ = 19 J/cm$^2$, and remained unchanged for the calculations at $F_{1\omega}$ = 24.5 J/cm$^2$ (other experimental fluence used in this study). Consequently, the dependence is given by $\Omega$ only, through the determination of $Q_{abs}$ for each position. In other words, this model is expected to reproduce the experimental results for any fluence $F_{1\omega}$ tested on this crystal.

### 3.1.3 Comparison model versus experiments: $\rho_{|F=cst} = f(\Omega)$ and $\rho = f(F_{1\omega})$

Through DDScat, the curve $Q_{abs} = f(\Omega)$ can be finally extracted which is then re-injected in DMT code to reproduce the curve $\rho_{|F=cst} = f(\Omega)$, i.e. the evolution of the laser damage density as a function of $\Omega$. Calculations have been performed turn by turn with the two geometric configurations previously presented. For each configuration, defects are considered as all oriented in the same direction comparatively to the laser beam. For the prolate geometry, $Q_{abs}$ variations are correlated to the variations of $\rho(\Omega)$. As regards the oblate one which has also been proposed, it has been immediately leaved out since variations introduced by the $Q_{abs}$ coefficient were anti-correlated to those obtained experimentally. Note that other geometries (not satisfying the condition $a = b$) have also been studied. Results (not presented here) show that either the variations of $Q_{abs}$ are anti-correlated or its variations are not large enough to reproduce experimental results whatever the $1\omega$ fluence.

On Fig. 5, green and orange dash lines respectively correspond to fluence $F_{1\omega}$ = 19 J/cm$^2$ and fluence $F_{1\omega}$ = 24.5 J/cm$^2$. As said in Sec. 3.1.1, one would note that it is important to dissociate the impact of the SHG on the damage density from the geometry effect due to the rotation angle Ω. For a modeling concern, it is thus not mandatory to include SHG as a contributor to laser damage. So, in the range [0°, 90°], one can clearly see that modeling is in good agreement with experimental results for both fluences. Moreover, given the error margins, only the points linked to SHG peaks are out of the model validity. Now considering the positions Ω = 0°and Ω = 90°, this modeling reproduces the experimental damage density as function of the fluence on the whole range of the scanned fluences. This approach, with the introduction of an ellipsoidal geometry, enables to reproduce the main experimental trends whereas modeling based on spherical geometry can not.

### 3.2 Multi-wavelength study: coupling of LID mechanisms

In the previous section, we have highlighted the effect of polarization on the laser damage resistance of KDP crystals. It has been demonstrated that precursor defects and more precisely their geometries could impact the physical mechanisms responsible for laser damage in such material. In Sec. 3.2, we are going to focus on the identification of these physical process. To do so, it is assumed that the use of multi-wavelengths damage test is an original way to discriminate the mechanisms due to their strong dependence as a function of the wavelength.

#### 3.2.1 Experimental results in the multi-wavelengths case

In the case of mono-wavelength tests, damage density evolves as a function of the fluence following a power law. As an example, this can be represented on Fig. 8 (a) for two tests carried out at 1$\omega$ and 3$\omega$. Mono-wavelength tests can be considered as the identity chart of the crystal. Note that the damage resistance of KDP is different as a function of the wavelength: the longer the wavelength, the better the crystal can resist to photon flux.
In the case of multi-wavelength tests, the damage density $\rho$ is thus extracted as a function of each couple of fluences ($F_{3\omega}$,$F_{1\omega}$). Fig. 8 (b) exhibits the evolution of $\rho(F_{3\omega},F_{1\omega})$, symbolized by color contour lines.

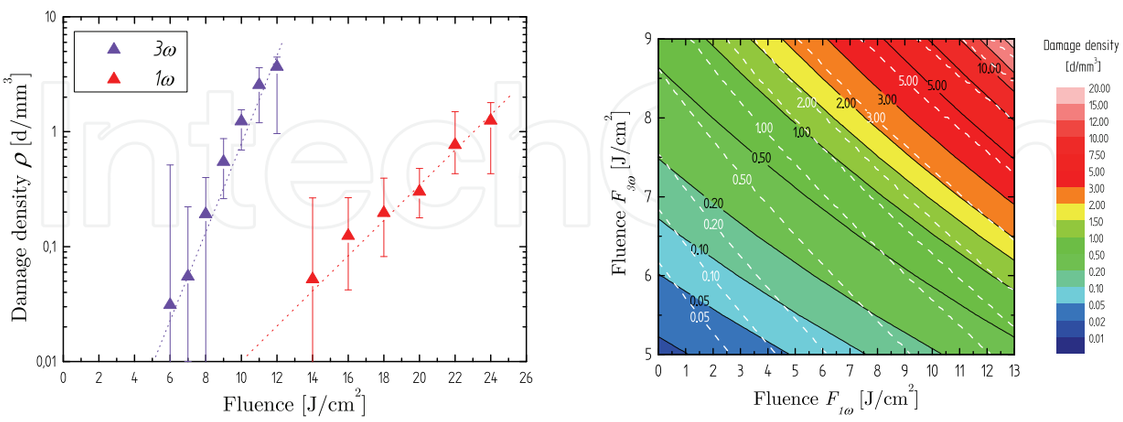


Fig. 8. (a) Damage density versus fluence in the mono-wavelength case: for 1$\omega$ and 3$\omega$. (b) Evolution of the LID densities (expressed in dam./mm$^3$) as a function of $F_{3\omega}$ and $F_{1\omega}$. The color levels stand for the experimental damage densities. Modeling results are represented in white dash contour lines for $\delta$ = 3. Modeling results are discussed in Sec. 3.2.3.

A particular pattern for the damage densities stands out. Indeed, each damage iso-density is associated to a combination between $F_{3\omega}$ and $F_{1\omega}$ fluences. If now we compare results obtained in the mono- and multi-wavelengths cases, it is possible to observe a coupling between the $3\omega$ and $1\omega$ wavelengths (Reyné et al., 2009). Indeed, we can observe that:

$$\rho = f(F_{3\omega}, F_{1\omega}) \neq \rho(F_{1\omega}) + \rho(F_{3\omega}) \tag{17}$$

On Fig. 8 (a), for $F_{3\omega}$ = 5 J/cm$^2$ and $F_{1\omega}$ = 10 J/cm$^2$, the resulting damage density (if we do the sum) would be $\rho = 2.10^{-2}$ d/mm$^3$. Whereas on Fig. 8 (b) for the same couple of fluences $F_{3\omega}$ and $F_{1\omega}$, the resulting damage density is $\rho = 2.10^{-1}$ d/mm$^3$, i.e. one order of magnitude higher. Other experimental results (DeMange et al., 2006) indicates that it is possible to predict the damage evolution of a KDP crystal when exposed to several different wavelengths from the damage tests results. It can be said that mono-wavelength results are necessary but not sufficient due to the existence of a coupling effect.
Besides, it is possible to define a $3\omega$-equivalent fluence $F_{eq}$, depending both on $F_{3\omega}$ and $F_{1\omega}$, which leads to the same damage density that would be obtained with a $F_{3\omega}$ fluence only. $F_{eq}$ can be determined using approximately a linear relation between $F_{3\omega}$ and $F_{1\omega}$, linked by a slope $s$ resulting in

$$F_{eq} = f(F_{3\omega}, F_{1\omega}) = sF_{1\omega} + F_{3\omega} \tag{18}$$

By evidence, $s$ contains the main physical information about the coupling process. Thus, in the following we focus our attention on this physical quantity. For $\rho \geq 3$ dam./mm$^3$, a constant value for $s_{exp}$ close to -0.3 is obtained from Fig. 8 (b).

#### 3.2.2 Model: introducing two wavelengths

To interpret these data, the DMT$_{2\lambda}$ code has been developed on the basis of the mono-wavelength DMT model. To address the multiple wavelengths case, the DMT$_{2\lambda}$ model takes into account the presence of two wavelengths at the same time: here the $3\omega$ and $1\omega$. For this configuration, a particular attention has been paid to the influence of the wavelength on the defects energy absorption.
First, a single population of defects is considered: the one that is used to fit the experimental densities at $3\omega$ only. Secondly, it is assumed that the temperature elevation results from a combination of each wavelength absorption efficiency such as

$$Q_{abs}^{(\omega)} I_{(\omega)} = Q_{abs}^{(3\omega)}(3\omega, 1\omega) I_{3\omega} + Q_{abs}^{(1\omega)}(3\omega, 1\omega) I_{1\omega} \tag{19}$$

Where $Q_{abs}^{(3\omega)}(3\omega, 1\omega)$ and $Q_{abs}^{(1\omega)}(3\omega, 1\omega)$ are the absorption efficiencies at $3\omega$ and $1\omega$. It is noteworthy that *a priori* each absorption efficiency depends on the two wavelengths since both participate into the plasma production. Thirdly, calculations are performed under conditions where the Rayleigh criterion ($a \leq 100$ nm) is satisfied: under this condition, an error less than 20 % is observed when the approximate expression of $Q_{abs}^{(\omega)}$ is used. So, $Q_{abs}^{(3\omega)}(3\omega, 1\omega)$ and $Q_{abs}^{(1\omega)}(3\omega, 1\omega)$ contain the main information about the physical mechanisms implied in LID.
According to a Drude model, $Q_{abs}^{(\omega)} \propto \epsilon_2 \propto n_e$ where $n_e$ is mainly produced by multiphoton ionization (MPI), $\epsilon_2$ representing the imaginary part of the dielectric function (Dyan et al., 2008). Indeed, electronic avalanche is assumed to be negligible (Dyan et al., 2008) at first glance. It follows that $n_e \propto F_{(\omega)}^{\delta}$ where $\delta$ is the multiphotonic order (Agostini & Petite, 88). For KDP crystals, at $3\omega$ three photons at 3.54 eV are necessary for valence electrons to break through the 7.8 eV band gap (Carr et al., 2003) whereas at $1\omega$ seven photons at 1.18 eV would

be required, lowering drastically the absorption cross-section. Then, it is assumed that $n_e = n_e^{(3\omega)} + n_e^{(1\omega)}$, where $n_e^{(3\omega)}$ and $n_e^{(1\omega)}$ are the electron densities produced by the $3\omega$ and $1\omega$ pulses. Here the interference between both wavelengths are neglected. This assumption is reliable since the conditions permit to consider that the promotion of valence electrons to the Conduction Band (CB) is mainly driven by the $3\omega$ pulse ($F_{3\omega} \geq 5$ J/cm$^2$). As a consequence, we consider that the $3\omega$ is the predominant wavelength to promote electrons in the CB.
So for the $3\omega$ it results that $Q_{abs}^{(3\omega)}(3\omega, 1\omega) = Q_{abs}^{(3\omega)}(3\omega)$ while for the $1\omega$, since $Q_{abs}^{(1\omega)} \propto n_e$ in the Rayleigh regime, the $1\omega$-energy absorption coefficient can be written as

$$Q_{abs}^{(1\omega)}(3\omega, 1\omega) = \beta F_{3\omega}^{\delta} + Q_{abs}^{(1\omega)} \tag{20}$$

$\beta$ is a parameter which is adjusted to obtain the best agreement with the experimental data. It is noteworthy that $\beta$ has no influence on the slopes $s$ predicted by the model. Finally, the $\mathrm{DMT}_{2\lambda}$ model is able to predict the damage densities $\rho(F_{3\omega}, F_{1\omega})$ from which the slope $s$ is extracted.

### 3.2.3 Modeling results

Fig. 9 represents the evolution of the modeling slopes $s$ as a function of $\delta$ for the damage density $\rho$ = 5 d/mm$^3$. One can see that the intersection between $s_{exp}$ and the modeling slopes is obtained for $\delta \simeq 3$. These calculations have also been performed for various iso-densities ranging from 2 to 15 d./mm$^3$.

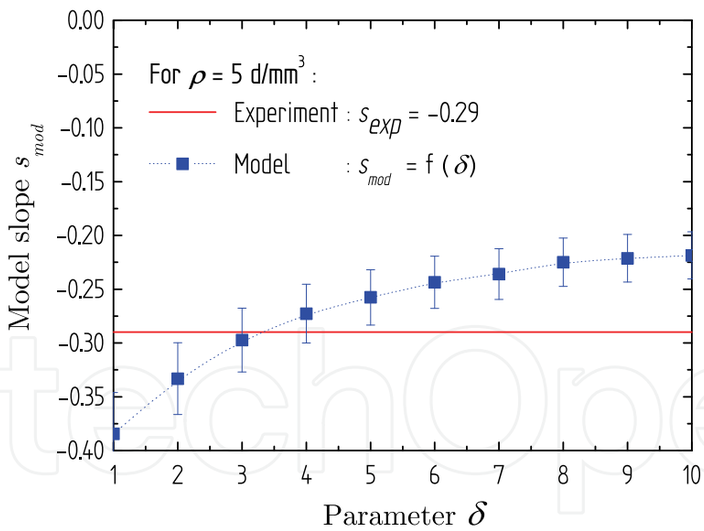


Fig. 9. Evolution of the modeling slopes $s$ as a function of $\delta$ for the damage iso-density $\rho$ = 5 d/mm$^3$. For this density level, the experimental slope is $s_{exp} \simeq -0.3$.

As a consequence, observations result in Fig. 10 which shows that $\delta \simeq 3$ for $\rho \geq 3$ d/mm$^3$. Actually, it is most likely that $\delta$ = 3 considering errors on the experimental fluences, uncertainties on the linear fit to obtain $s_{exp}$, and owing to the band gap value. Therefore, the comparison between this experiment and the model indicates that the free electron density leading to damage is produced by a three-photon absorption mechanism. It is noteworthy

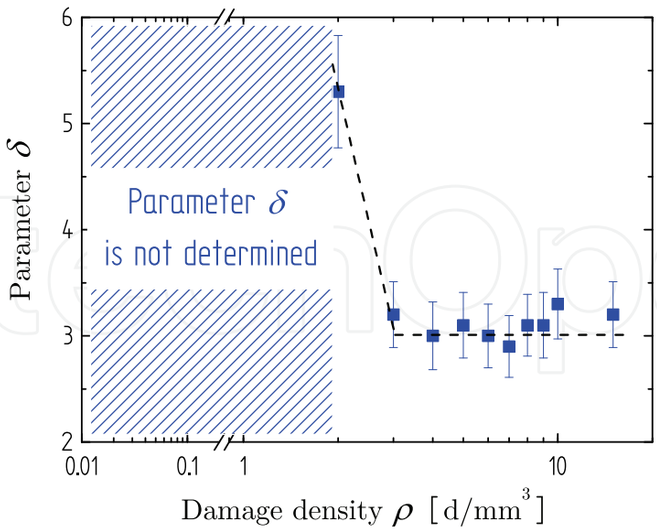


Fig. 10. Evolution of the best parameter $\delta$ which fits the experimental slope $s_{exp}$, as a function of $\rho$. Given a damage density, the error bars are obtained from the standard deviation observed between the minimum and maximum slopes.

that this absorption is assisted by defects that induce intermediate states in the band gap (Carr et al., 2003).
Finally, as reported in Fig. 8 (b) the trends given by this model (plotted in white dashes) are in good agreement with the experimental results for $\rho \geq 3$ d/mm$^3$.
However, this model cannot reproduce the experimental trends on the whole range of fluences and particularly fails for the lowest damage densities. To explain the observed discrepancy, two explanations based on the defects size are proposed. First, it has been suggested that the defects size may impact on the laser damage mechanisms. For the lowest densities, the size distribution (Feit & Rubenchik, 2004) used to calculate the damage densities implies larger defects (i.e. $a \geq 100$ nm). Thus, it oversteps the limits of the Rayleigh criterion: indeed, an error on $Q_{abs}$ larger than several tens of percents is observed when $a \geq 100$ nm.
Secondly, the contribution of larger size defects which is responsible for the lowest densities may also be consistent with an electronic avalanche competing with the MPI dominant regime. Indeed, for a given density $n_e$ produced by MPI, since avalanche occurs provided that it exists at least one free electron in the defect volume (Noack & Vogel, 1999), the largest defects are favorable to impact ionization. Once engaged, avalanche enables an exponential growth of $n_e$ (which is assumed to be produced by the $F_{3\omega}$ fluence essentially). Mathematically, the development of this exponential leads to high exponents of the fluence which is then consistent with $\delta > 5$ or more. In Fig. 10, it corresponds to the hashed region where the modeling slopes do not intercept the experimental ones.
In other respects, the nature of the precursor defects has partially been addressed in the mono-wavelength configuration (DeMange et al., 2008; Feit & Rubenchik, 2004; Reyné et al., 2009). In the DMT$_{2\lambda}$ model, we consider a single distribution of defects, corresponding to a population of defects both sensitive at $3\omega$ and $1\omega$. Calculations with two distinct distributions have also been performed. It comes out that no significant modification is observed between the results obtained with only one distribution: e.g. the damage densities pattern nearly

remains unchanged and the slopes $s$ as well. Also these observations do not dismiss that two populations of defects may exist in KDP (DeMange et al., 2008).

## 4. Conclusion

The laser-induced damage of optical components used in megajoule-class lasers is still under investigation. Progress in the laser damage resistance of optical components has been achieved thanks to a better understanding of damage mechanisms. The models proposed in this study mainly deal with thermal approaches to describe the occurrence of damage sites in the bulk of KDP crystals. Despite the difficulty to model the whole scenario leading to damage initiation, these models account for the main trends of KDP laser damage in the nanosecond regime.

Based on these thermal approaches, direct comparisons between models and experiments have been proposed and allow: *(i)* to obtain some main information on precursor defects and their link to the physical mechanisms involved in laser damage and *(ii)* to improve our knowledge in LID mechanisms on powerful laser facilities.

## 5. References

Adams, J., Weiland, T., Stanley, J., Sell, W., Luthi, R., Vickers, J., Carr, C., Feit, M., Rubenchik, A., Spaeth, M. & Hackel, R. (2005). Pulse length dependence of laser conditioning and bulk damage in $KD_2PO_4$, *Proc. SPIE 5647*, p. 265.

Agostini, P. & Petite, G. (1988). Photoelectric effect under strong irradiation, *Contemporary Physics* 29: 55–77.

Bliss, E. (1971). Pulse duration dependence of laser damage mechanism, *Opto-electronics* 3: 99.

Burnham, A., Runkel, M., Feit, M., Rubenchik, A., Floyd, R., Land, T., Siekhaus, W. & Hawley-Fedder, R. (2003). Laser-induced damage in deuterated potassium dihydrogen phosphate, *Appl. Opt.* 42, 27: 5483–5495.

Carr, C., Radousky, H. & Demos, S. (2003). Wavelength dependence of laser-induced damage: determining the damage initiation mechanisms, *Phys. Rev. Lett.* 91, 12: 127402.

Carr, C., Radousky, H., Rubenchik, A., Feit, M. & Demos, S. (2004). Localized dynamics during laser-induced damage in optical materials, *Phys. Rev. Lett.* 92, 8: 087401.

Carslaw, H. & Jaeger, J. (1959). *Conduction of heat in solids*, Oxford Science Publications (2nd ed.).

Van de Hulst, H. C. (1981). *Light scattering by small particles*, Dover publications Inc., New York.

DeMange, P., Negres, R. & Rubenchick, A. (2006). Understanding and predicting the damage performance of $K_2H_{(2-x)}D_xPO_4$ crystal under simultaneous exposure to 532- and 355-nm pulses, *Appl. Phys. Lett.* 89: 181922.

DeMange, P., Negres, R., Rubenchik, A., Radousky, H., Feit, M. & Demos, S. (2008). The energy coupling efficiency of multiwavelenght laser pulses to damage initiating defects in deuterated $KH_2PO_4$ nonlinear crystals, *J. Appl. Phys.* 103: 083122.

Demos, S., DeMange, P., Negres, R. & Feit, M. (2010). Investigation of the electronic and physical properties of defect structures responsible for laser-induced damage in DKDP crystal, *Opt. Express* 18, 12: 13788–13804.

Demos, S., Staggs, M. & Radousky, H. (2003). Bulk defect formations in $KH_2PO_4$ crystals investigated using fluorescence microscopy, *Phys. Rev. B* 67: 224102.

Draine, B. & Flatau, P. (1994). Discrete-dipole approximation for scattering calculations, *J. Opt. Soc. Am. B* 11: 1491–1499.

Draine, B. & Flatau, P. (2008). The discrete dipole approximation for periodic targets: theory and tests, *J. Opt. Soc. Am. A* 25: 2693–2703.

Draine, B. & Flatau, P. (n.d.). *User guide for the discrete dipole approximation code DDScat 7.0*.

Duchateau, G. (2009). Simple models for laser-induced damage and conditioning of potassium dihydrogen phosphate crystals by nanosecond pulses, *Opt. Express* 17, 13: 10434–10456.

Duchateau, G. & Dyan, A. (2007). Coupling statistics and heat transfer to study laser-induced crystal damage by nanosecond pulses, *Opt. Express* 18, 8: 4557–4576.

Dyan, A., Enguehard, F., Lallich, S., Piombini, H. & Duchateau, G. (2008). Scaling laws in laser-induced KDP crystal damage by nanosecond pulses at $3\omega$, *J. Opt. Soc. Am. B* 25, 6: 1087–1095.

Feit, M. & Rubenchik, A. (2004). Implications of nanoabsorber initiators for damage probability curves and pulselength scaling and laser conditioning, *Proc. SPIE 5273*, pp. 527374–82.

Gallais, L., Natoli, J. & Amra, C. (2002). Statistical study of single and multiple pulse laser-induced damage in glasses, *Opt. Express* 10: 1465–1474.

Gallais, L., Voarino, P. & Amra, C. (2004). Optical measurement of size and complex index of laser-damage precursors: the inverse problem, *J. Opt. Soc. Am. B* 21: 1073–1080.

Hopper, R. & Uhlmann, D. (1970). Mechanism of inclusion damage in laser glass, *J. Appl. Phys.* 41, 10: 4023–4037.

Hummel, R. (2001). *Electronic properties of materials*, Springer and Third Edition.

*ISO Standard No 11254-1:2000; ISO Standard No 11254-2:2001* (2001).

Lamaignère, L., Donval, T., Loiseau, M., Poncetta, J., Razé, G., Meslin, C., Bertussi, B. & Bercegol, H. (2009). Accurate measurements of laser-induced bulk damage density, *Meas. Sci. Technol.* 20: 095701.

Liu, C., Kioussis, N., Demos, S. & Radousky, H. (2003). Electron- or hole-assisted reactions of H defects in hydrogen-bonded KDP, *Phys. Rev. Lett.* 91, 1: 015505.

Liu, C., Zhang, Q., Kioussis, N., Demos, S. & Radousky, H. (2003). Electronic structure calculations of intrinsic and extrinsic hydrogen point defects in $KH_2PO_4$, *Phys. Rev. B* 68, 22: 224107.

Natoli, J., Gallais, L., Akhouayri, H. & Amra, C. (2002). Laser-induced damage of materials in bulk and thin film and and liquid forms, *App Opt.* 41, 16: 3156–3166.

Noack, J. & Vogel, A. (1999). Laser-induced plasma formation in water at nanosecond to femtosecond time scales: calculation of thresholds, absorption coefficients, and energy density, *IEEE J. Quant. Electron.* 35: 1156–1167.

*Numerical Recipies* (n.d.).

O'Connell, R. (1992). Onset threshold analysis of defect-driven surface and bulk laser damage, *Appl. Optics* 31, 21: 4143.

Picard, R., Milam, D. & Bradbury, R. (1977). Statistical analysis of defect-caused laser damage in thin films, *Appl. Opt.* 16: 1563–1571.

Pommiès, M., Damiani, D., Bertussi, B., Piombini, H., Mathis, H., Capoulade, J. & Natoli, J. (2006). Detection and characterization of absorption heterogeneities in $KH_2PO_4$ crystals, *Opt. Comm.* 267: 154–161.

Porteus, J. & Seitel, S. (1984). Absolute onset of optical surface damage using distributed defect ensembles, *Appl. Optics* 23, 21: 3796–3805.

Reyné, S., Duchateau, G., Natoli, J.-Y. & Lamaignère, L. (2009). Laser-induced damage of KDP crystals by 1$\omega$ nanosecond pulses: influence of crystal orientation, *Opt. Express* 17, 24: 21652–21665.

Reyné, S., Duchateau, G., Natoli, J.-Y. & Lamaignère, L. (2010). Pump-pump experiment in $KH_2PO_4$ crystals: Coupling two different wavelengths to identify the laser-induced damage mechanisms in the nanosecond regime, *Appl. Phys. Lett.* 96: 121102–121104.

Reyné, S., Loiseau, M., Duchateau, G., Natoli, J.-Y. & Lamaignère, L. (2009). Towards a better understanding of multi-wavelength effects on KDP crystals, *Proc. SPIE 7361*, p. 73610Z.

Sparks, M., Mills, D., Warren, R., Holstein, T., Maradudin, A., Sham, L., Loh, E., Jr. & King, D. (1981). Theory of electron-avalanche breakdown in solids, *Phys. Rev. B* 24, 6: 3519–3536.

Stuart, B., Feit, M., Herman, S., Rubenchik, A., Shore, B. & Perry, M. (1996). Nanosecond-to-femtosecond laser-induced breakdown in dielectrics, *Phys. Rev. B* 53, 4: 1749.

Trenholme, J., Feit, M. & Rubenchik, A. (2006). Size-selection initiation model extended to include shape and random factors, *Proc. SPIE 5991*, p. 59910X.

Walker, T., Guenther, A. & Nielsen, P. (1981). Pulsed laser-induced damage to thin film optical coatings - part 2: Theory, *IEEE J. Quantum Electron.* QE-17, 10: 2053.

Wang, K., Fang, C., Zhang, J., Liu, C., Boughton, R., Wang, S. & Zhao, X. (2005). First-principles study of interstitial oxygen in potassium dihydrogen phosphate crystals, *Phys. Rev. B* 72: 134110.

Wood, R. (2003). *Laser-induced damage of optical materials*, Institute Of Physics publishing series in optics ans optoelectronics, Bristol and Philadelphia.

Zaitseva, N., Atherton, J., Rozsa, R., Carman, L., Smolsky, I., Runkel, M., Ryon, R. & James, L. (1999). Design and benefits of continuous filtration in rapid growth of large KDP and DKDP crystals, *J. Crystal Growth* 97, 4: 911–920.

Zaitseva, N., Carman, L., Smolsky, I., Torres, R. & Yan, M. (1999). The effect of impurities and supersaturation on the rapid growth of KDP crystals, *J. Crystal Growth* 204, 4: 512.

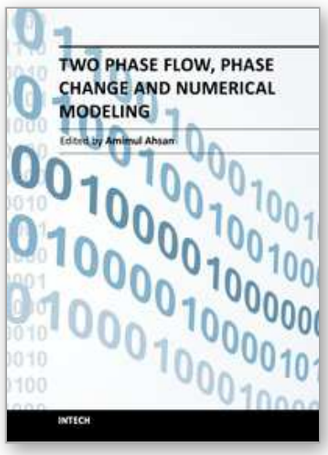


**Two Phase Flow, Phase Change and Numerical Modeling**
Edited by Dr. Amimul Ahsan

ISBN 978-953-307-584-6
Hard cover, 584 pages
**Publisher** InTech
**Published online** 26, September, 2011
**Published in print edition** September, 2011

The heat transfer and analysis on laser beam, evaporator coils, shell-and-tube condenser, two phase flow, nanofluids, complex fluids, and on phase change are significant issues in a design of wide range of industrial processes and devices. This book includes 25 advanced and revised contributions, and it covers mainly (1) numerical modeling of heat transfer, (2) two phase flow, (3) nanofluids, and (4) phase change. The first section introduces numerical modeling of heat transfer on particles in binary gas-solid fluidization bed, solidification phenomena, thermal approaches to laser damage, and temperature and velocity distribution. The second section covers density wave instability phenomena, gas and spray-water quenching, spray cooling, wettability effect, liquid film thickness, and thermosyphon loop. The third section includes nanofluids for heat transfer, nanofluids in minichannels, potential and engineering strategies on nanofluids, and heat transfer at nanoscale. The forth section presents time-dependent melting and deformation processes of phase change material (PCM), thermal energy storage tanks using PCM, phase change in deep CO2 injector, and thermal storage device of solar hot water system. The advanced idea and information described here will be fruitful for the readers to find a sustainable solution in an industrialized society.

**How to reference**
In order to correctly reference this scholarly work, feel free to copy and paste the following:

S. Reyné, L. Lamaignère, J-Y. Natoli and G. Duchateau (2011). Thermal Approaches to Interpret Laser Damage Experiments, Two Phase Flow, Phase Change and Numerical Modeling, Dr. Amimul Ahsan (Ed.), ISBN: 978-953-307-584-6, InTech, Available from: http://www.intechopen.com/books/two-phase-flow-phase-change-and-numerical-modeling/thermal-approaches-to-interpret-laser-damage-experiments

INTECH
open science | open minds

**InTech Europe**
University Campus STeP Ri
Slavka Krautzeka 83/A
51000 Rijeka, Croatia
Phone: +385 (51) 770 447
Fax: +385 (51) 686 166
www.intechopen.com

**InTech China**
Unit 405, Office Block, Hotel Equatorial Shanghai
No.65, Yan An Road (West), Shanghai, 200040, China
中国上海市延安西路65号上海国际贵都大饭店办公楼405单元
Phone: +86-21-62489820
Fax: +86-21-62489821

IntechOpen